Supplementary Information

Van der Waals-Bonded Graphene Clusters Enhance Thermal Conductivity of Phase-Change Materials for Advanced Thermal Energy Management

Liwen Sun,[‡ab] Yandong Wang,[‡ab] Lu Chen,[ab] Junfeng Ying,[ab] Qiuyu Li,[ab] Li Fu,[c] Qingwei Yan,[ab] Kai Wu,[d] Chen Xue,[*ab] Jinhong Yu,[ab] Nan Jiang,[ab] Kazuhito Nishimura,[e] Cheng-Te Lin[*ab] and Wen Dai[*ab]

[a] *Key Laboratory of Advanced Marine Materials, Ningbo Institute of Materials Technology and Engineering, Chinese Academy of Sciences, Ningbo 315201, P.R. China*

[b] *Center of Materials Science and Optoelectronics Engineering, University of Chinese Academy of Sciences, Beijing 100049, P.R. China.*

[c] *College of Materials and Environmental Engineering, Hangzhou Dianzi University, Hangzhou 310018, P. R. China.*

[d] *College of Polymer Science and Engineering, State Key Laboratory of Polymer Materials Engineering, Sichuan University, Chengdu 610065, P. R. China.*

[e] *Advanced Nano-processing Engineering Lab, Mechanical Systems Engineering, Kogakuin University, Tokyo 192-0015, Japan.*

[‡] *These authors contributed equally to this work.*

* Corresponding authors. *E-mail addresses*: xuechen@nimte.ac.cn (C. Xue); linzhengde@nimte.ac.cn (C. -T. Lin); daiwen@nimte.ac.cn (W. Dai)

This file includes:

Other Supplementary Materials for this manuscript includes the following:

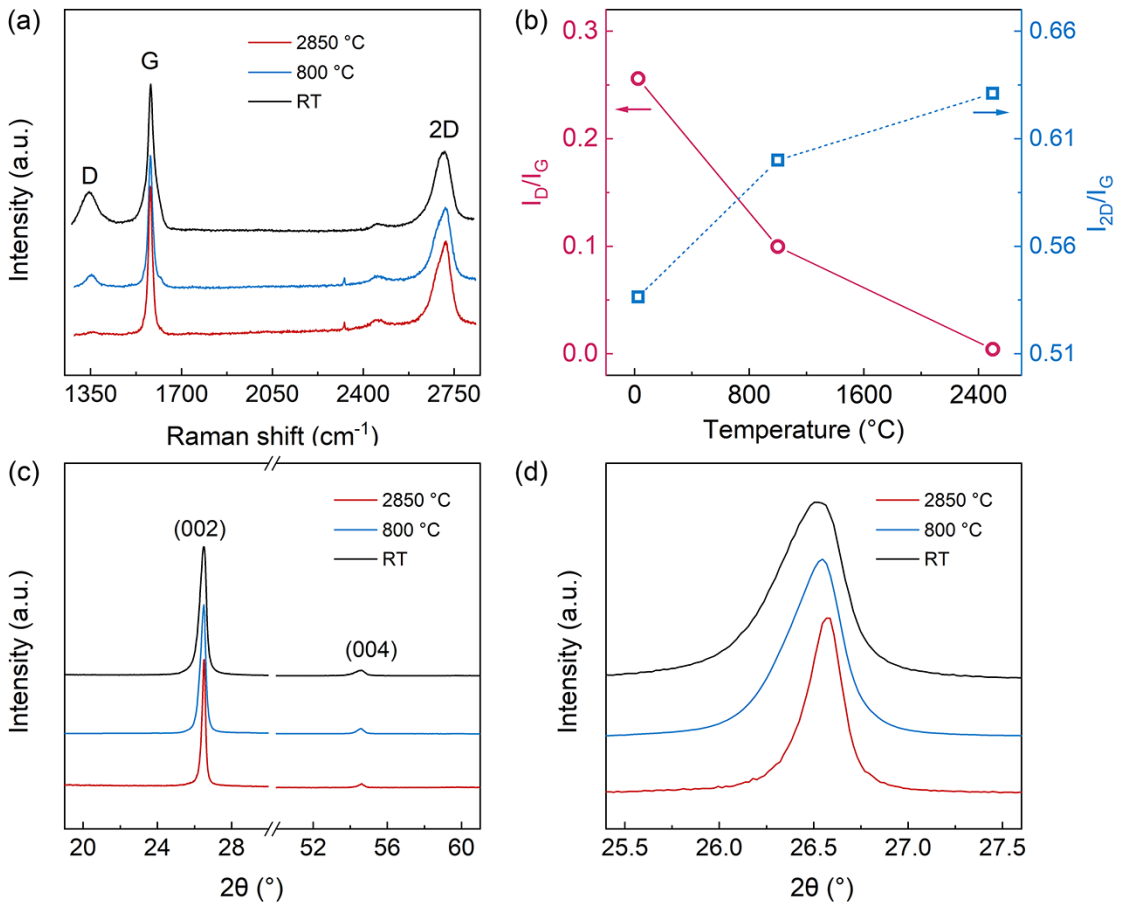

Fig. S1 (a) Raman spectra of raw graphene sheets (black line), graphene framework prepared by the pyrolysis of the graphene attached porous PU at 800 °C (blue line), and graphene clusters annealed at 2800 °C (red line). (b) The calculated I_D/I_G and I_{2D}/I_G ratios from (a). The decrease in I_D/I_G ratios and the increase in I_{2D}/I_G ratios signify the restoration of structural defects in graphene following high-temperature treatment.[S1,S2] (c and d) XRD patterns of the three samples. The narrower width of the (002) peak implies an enlargement in the domain size of graphene along the basal planes after high-temperature treatment.[S3,S4]

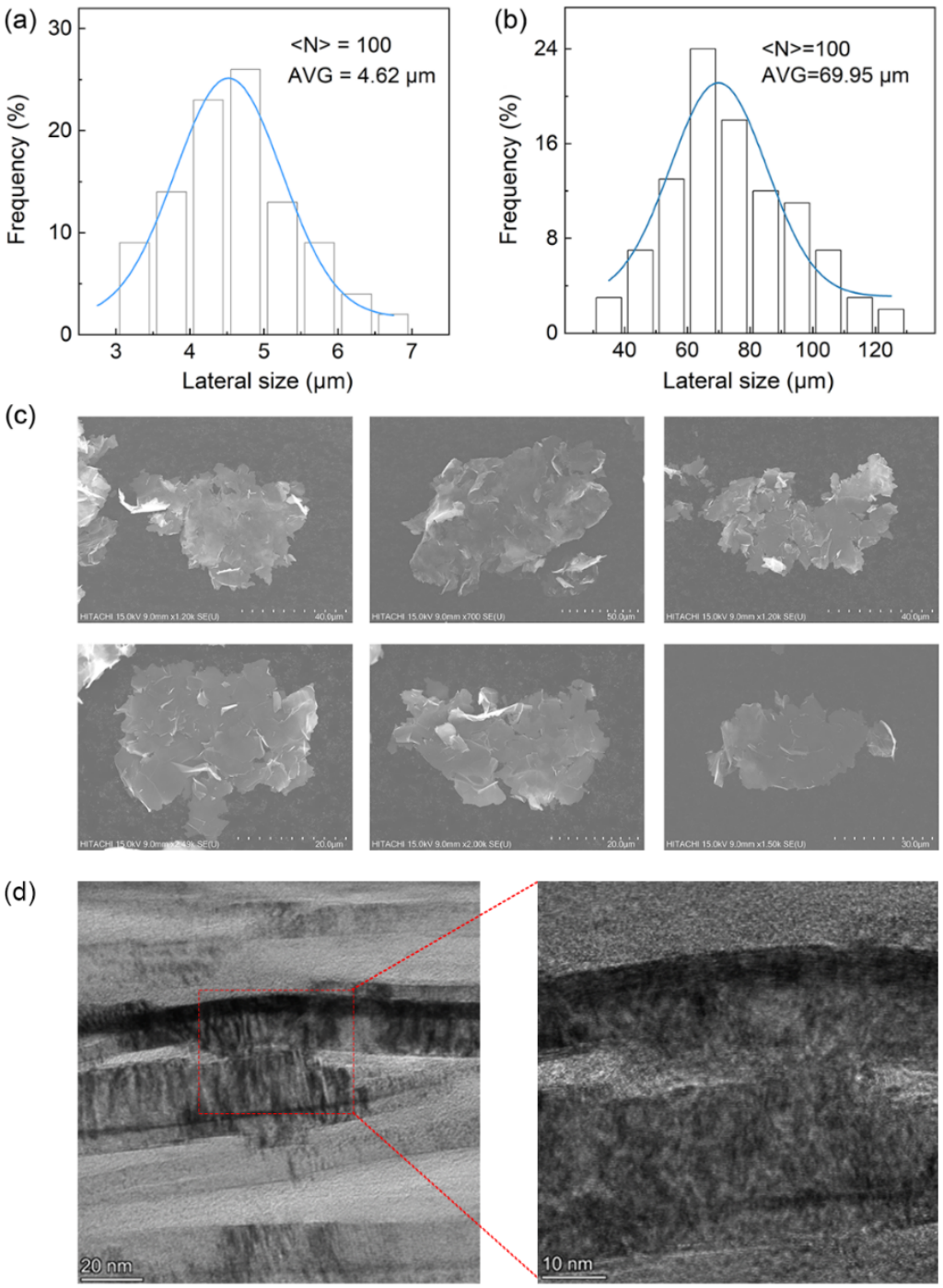

Fig. S2 Size statistical histograms of (a) the raw graphene sheets and (b) the as-prepared graphene clusters. (c) Some typical morphologies of graphene clusters. (d) TEM images illustrating vdW-bonded interfaces of adjacent graphene sheets.

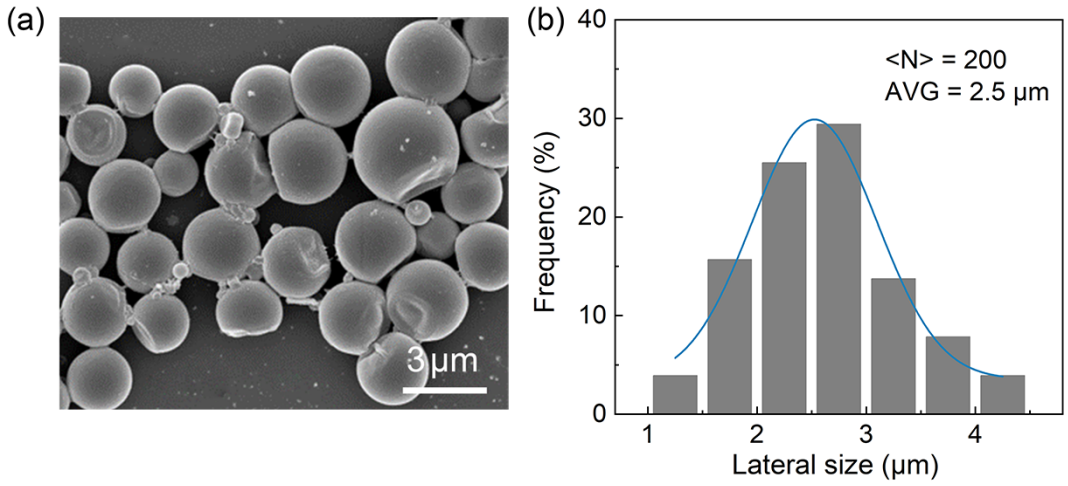

Fig. S3 (a) Typical SEM image and (b) the size statistical histograms of PCMC.

Section S1 Thermal conductivity analysis of the VBGC/PCMCs and GS/PCMC composites using the *Agari* heat conduction model.

For composites comprising fillers and a polymer matrix, the thermal conductivity for the ideal parallel and series models can be estimated using Equations (1) and (2), respectively.

$$\kappa_{com} = f \times \kappa_{filler} + (1 - f) \times \kappa_{matrix} \quad (1)$$

$$(\kappa_{com})^{-1} = f \times (\kappa_{filler})^{-1} + (1 - f) \times (\kappa_{matrix})^{-1} \quad (2)$$

Here, κ_{com}, κ_{filler}, and κ_{matrix} represent the thermal conductivity of the composite, filler, and polymer matrix, respectively; [f] is the volume fraction of the filler. Given the commonality of Equations (1) and (2), a general Equation (3) can be formulated:

$$(\kappa_{com})^{n} = f \times (\kappa_{filler})^{n} + (1 - f) \times (\kappa_{matrix})^{n} \quad (3)$$

In Equation (3), if n equals 1 or -1, it corresponds to Equation (1) and Equation (2), respectively. Generally, -1 < n < 1. Equation (3) is a comprehensive formula for both parallel and series models, and it is derived under the assumption that the filler forms a fully continuous structure within the matrix. However, in practical scenarios, fillers may be dispersed in the matrix or create a continuous pathway. As a result, the effective thermal conductivity of fillers in composites is typically lower than their intrinsic thermal conductivity. Following *Agari*'s theory, the index [n] can be replaced by the index [$C \cdot$ n], leading to the conversion of Equation (3) into Equation (4):[S5]

$$(\kappa_{com})^{n} = f \times (\kappa_{filler})^{C \cdot n} + (1 - f) \times (\kappa_{matrix})^{n} \quad (4)$$

In this equation, [C] represents a parameter used to assess the thermal percolation pathway formed by contacting fillers. The closer [C] is to 1, the higher the heat transfer efficiency of the pathway.

In the case of VBGC/PCMCs, Equation (4) can be transformed into Equation (5), where κ_{pre}, κ_{filler}, and κ_{PCMC} represent the thermal conductivity of the VBGC/PCMCs, applied fillers, and the PCMC,

respectively. Additionally, [f] denotes the volume fraction, and [n] is a parameter indicating the series and parallel components in the model.

$$(\kappa_{pre})^n = f \times (\kappa_{filler})^{C \cdot n} + (1 - f) \times (\kappa_{PCMC})^n \quad (5)$$

In the VBGC/PCMCs, the thermal conductivity of PCMC (0.5 W m^{-1} K^{-1}) is significantly lower than that of graphene sheets (10^3 W m^{-1} K^{-1}), leading to its minimal contribution to the overall thermal conductivity of the composites (κ_{pre}). Hence, to simplify Equation (5) further and derive the index [n], we exclude the second term on the right-hand side of this equation. This leads to Equation (5) conversion into Equation (6).

$$(\kappa_{pre} - \kappa_{PCMC})^n = f \times (\kappa_{filler})^{C \cdot n} \quad (6)$$

where ($\kappa_{\text{pre}} - \kappa_{\text{PCMC}}$) specifically accounts for the increase in thermal conductivity of composites due to graphene fillers. To solve this nonlinear function, we apply a logarithm to both sides of Equation (6), resulting in the derivation of Equations (7) and (8):

$$n\log(\kappa_{pre} - \kappa_{PCMC}) = \log f + C \cdot n\log(\kappa_{filler}) \quad (7)$$

$$\log(\kappa_{pre} - \kappa_{PCMC}) = \frac{1}{n}\log f + C \cdot \log(\kappa_{filler}) \quad (8)$$

$$\kappa_{filler} = \kappa_{graphene\ sheets} \times \langle \cos^2 \theta \rangle \quad (9)$$

In the analysis of this thermal conductivity model, we focused on graphene sheets as the subject of study. To address the potential impact of directional arrangement differences, Equation (9) is introduced.

Accordingly, we employed Equation (8 and 9) to fit the experimental thermal conductivity of VBGC/PCMCs and GS/PCMCs. The results are presented in Fig. S4, where the independent variable is [log$f$], the dependent variable is log ($\kappa_{\text{pre}} - \kappa_{\text{PCMC}}$), the slope is [1/n], and the intercept is [C log ($\kappa_{\text{graphene sheets}}$)]. Based on the results of this linear fit, we can calculate that the mean value of the

index [n] is 0.616 for VBGC/PCMCs and 0.957 for GS/PCMCs. By substituting the calculated values of [n] into Equation (8 and 9), we can compute the [*C*] values for VBGC/PCMCs and GS/PCMCs at different filler content, as shown in Table S1.

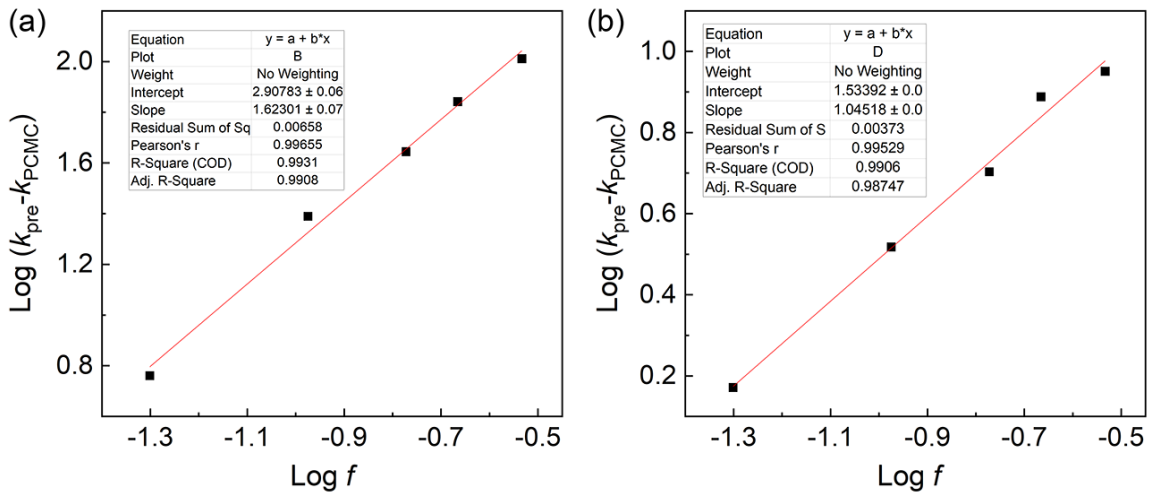

Fig. S4 The fitting results of the thermal conductivity for (a) VBGC/PCMCs and (b) GS/PCMCs based on Equation (8 and 9).

Table S1 The calculated parameter [*C*] of the VBGC/PCMCs and GS/PCMCs based on above analysis.

Filler content	5.0 vol%	10.6 vol%	16.9 vol%	21.6 vol%	29.3 vol%
VBGC/PCMCs	0.975	1.008	0.983	0.991	0.976
GS/PCMC	0.545	0.547	0.537	0.563	0.537

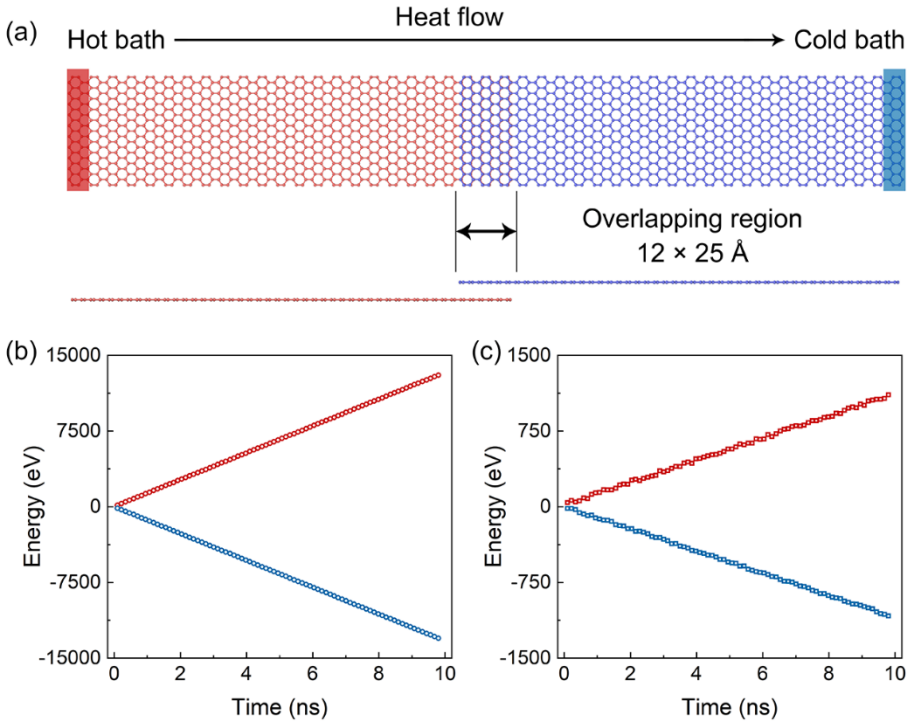

Fig. S5 (a) Schematic of the NEMD implementation for the calculation of the junction thermal conductance of the adjacent graphene sheets. The calculated heat flux across the two-layer graphene junction structure: (b) for the vdW-bonded interface, and (f) the interface formed based on non-bonding vdW interactions.

To comprehensively investigate the impact of inter-layer interactions between adjacent graphene sheets on thermal performance, non-equilibrium molecular dynamics (NEMD) simulations were conducted. As the simulation model shown in Fig. S5a, each graphene sheet has a lateral size of 100 Å × 25 Å. In order to calculate the junction thermal conductance between adjacent graphene sheets, we set two graphene sheets to overlap each other, with an overlapping region of 12 Å × 25 Å. The simulations were performed using the LAMMPS molecular dynamics simulator, in which the optimized *Tersoff* potential was employed to characterize intralayer C-C interactions, while the *Lennard-Jones* potential was utilized to describe interlayer C-C interactions.[S6,S7] To calculate the thermal performance differences between the vdW-bonded interface and the interface formed based on non-bonding vdW interactions, we varied the settings of well-depth energy (ε) and equilibrium

distance (σ) associated with the potential energy functions in the two models. Based on previous reports, for the vdW-bonded interface, ε is set to 4.6 meV, and σ is set to 0.335 nm.[S8] For the interface formed based on non-bonding vdW interactions, ε is 2.4 meV, and σ is 0.34 nm.[S9]

Initially, periodic boundary conditions are implemented across all dimensions, and atoms are assigned random velocities that reflect an average kinetic energy of 5 K, based on a Gaussian distribution. This is followed by a structural relaxation phase within the NPT ensemble (isobaric-isothermal condition), where N represents a constant number of atoms, P denotes constant pressure, and T signifies constant temperature, all maintained at 0 Pa and 300 K, respectively. After the relaxation process, to ensure stability, a few atomic layers at each end of the simulation domain are fixed. Finally, the atoms within the hot (cold) bath undergo a rescaling process to attain a temperature of 320 K (280 K) at each timestep, spanning a total simulation duration of 10 ns. Throughout this period, the temperature distribution and heat flux of the systems are meticulously recorded.

As the temperature distribution in Fig. 3m (in the manuscript), the average temperature drop (ΔT) is 15.7 K for the vdW-bonded interface, lower than 26.1 K for the interface formed based on non-bonding vdW interactions. In Fig. S5b – c, the heat flux across the two-layer graphene junction structure in the former case (1330.2 eV/ns) is considerably greater than that observed in the latter (109.9 eV/ns). To quantify the impact of interface interactions between adjacent graphene layers and the thermal conductance, we computed the junction thermal conductance (κ_{junction}) using Equation (10):

$$\kappa_{\text{junction}} = \frac{q}{S_{\text{junction}}\Delta T} \tag{10}$$

where q is the heat current that flows across the system from the hot bath to the cold one; ΔT is the temperature drop between the two sides of the overlapping region; S_{junction} is the overlapping area of the two-layer graphene junction structure along the heat current direction (12 Å × 25 Å).

As a result, we determined that the κ_{junction} at the vdW-bonded interface (4.54×10^9 W m^{-2} K^{-1}) is approximately 20 times higher than the interface formed through non-bonding vdW interactions

(2.25×10^8 MW m^{-2} K^{-1}).

Section S2 Thermal conductivity analysis of the VBGC/PCMCs and GS/PCMC composites employing the Foygel heat conduction model.

The *Foygel* heat conduction model was utilized to analyze the thermal conductivity of VBGC/PCMCs containing interconnected fillers, in accordance with Equation (11):[S10,S11]

$$\kappa_{pre} - \kappa_{PCMC} = \kappa_0 \left(\frac{f - f_c}{1 - f_c} \right)^{\tau} \tag{11}$$

Here, κ_{pre} represents the thermal conductivity of the VBGC/PCMCs as a function of the volume fraction [f], κ_{PCMC} is the thermal conductivity of the PCMC matrix, [κ_0] is a pre-exponential factor ratio associated with the contribution of fillers, [f_c] is the critical volume fraction of VBGCs, and [τ] is a conductivity exponent.

To solve this nonlinear function, a natural logarithm was applied to both sides of Equation (11), as demonstrated in Equation (12):

$$\ln\left(\kappa_{pre} - \kappa_{PCMC}\right) = \ln \kappa_0 + \tau \ln\left(f - f_c\right) - \tau \ln\left(1 - f_c\right) \tag{12}$$

In this context, [$\ln(\kappa_{pre} - \kappa_{PCMC})$] serves as the dependent variable, with the volume fraction [f] acting as the independent variable. Both [$\ln(\kappa_0)$] and [$\tau\ln(1–f_c)$] are constant terms. Consequently, Equation (13) is derived by taking the derivative of Equation (11). Subsequently, [τ] can be calculated based on Equation (14).

$$\frac{1}{\kappa_{com} - \kappa_{EP}} \times \frac{d\kappa_{com}}{df} = \frac{\tau}{f - f_c} \tag{13}$$

$$\tau = \frac{f - f_c}{\kappa_{com} - \kappa_{EP}} \times \frac{d\kappa_{com}}{df} \tag{14}$$

For the case of VBGC/PCMCs, the critical volume fraction, [f_c], is approximately 11%. This determination is made by analyzing the variation trend of experimental thermal conductivity [κ_{pre}] with the volume fraction [f], based on previous reports. [S11]

To elucidate the calculation process of $[\tau]$ and $[\kappa_0]$ for VBGC/PCMCs at the filler content of 29 vol%, we have meticulously documented the corresponding parameters (f and κ_{pre}) in Table S2 Then, based on the fitting curve plotted in Fig. 3j, the $\left.\frac{d\kappa_{pre}}{df}\right|_{f=29\%} = 638$ can be calculated. Applying Equation (14) and Equation (11), the values of $[\tau]$ and $[\kappa_0]$ for VBGC/PCMC (29 vol%) are determined to be 1.138 and 621, respectively.

Table S2. The parameters obtained from the *Foygel* model, and the calculated junction thermal conductivity.

	f (vol%)	κ_{com} (W m^{-1} K^{-1})	τ	κ_0	$R_{junction}$ (K W^{-1})
VBGC/PCMCs	29	103	1.138	621	284
GS/PCMCs	29	9.4	0.624	23.9	35824

Utilizing the acquired $[\kappa_0]$, $[f_c]$, and $[\tau]$ values as provided in Table S2, the junction thermal resistance ($R_{junction}$) between adjacent VBGC can be calculated with Equation (14), where L represents the lateral size of the VBGC (69.9 μm).

$$R_{junction} = \frac{1}{\kappa_0 L (f_c)^{\tau}} \quad (14)$$

Through the same analysis and calculation process, these parameters of GS/PCMCs can also be computed, and the results are listed in Table S2.

Table S3 Comparison of thermal conductivities of VBGC/PCMCs with reported graphene/polymer composites.

Filler	Matrix	κ_{pre} (W m^{-1} K^{-1})	f (vol%)	Ref.
Lamellar-structured graphene aerogels	Epoxy	20	2.3	S12
Graphene aerogels	1-octadecanol	4.28	2	S13
Graphene aerogels	Epoxy	6.57	0.54	S14
Graphene networks	PDMS	2.19	1.2	S15
Graphene aerogels	Paraffin wax	8.87	1.5	S16
Graphene aerogels (GO/GNP)	PEG	1.43	1	S17
Graphene networks	Epoxy	2.13	0.92	S18
Graphene woven fabrics	PI	3.73	7.7	S19
Graphene aerogels (GO/GNP)	Epoxy	5.92	5.5	S20
GNPs	Octadecanol	7.3	9.1	S21
Aligned carbon nanotube	Polycarbonate	4.87	16	S22
Graphene	Epoxy	6.9	27.4	S23
Arranged Ni-template graphene foam	Epoxy	11.16	6.2	S24
Ni templated 3D graphene	Natural rubber	8.8	4.87	S25
RGO/BN hybrid aerogel	Epoxy	11.01	25.4	S26
Graphene framework	Epoxy	10	3.19	S27
Vertically aligned graphene foam	Epoxy	35.5	19	S28
Multilayer graphene	Epoxy	1.5	2.8	S29
Ultrathin graphite foams-CNT	Epoxy	4.1	1.25	S30
Graphene-SiCNWs	Erythritol	2.63	6.54	S31
Graphene Nanoflake	Polyimide	10	25	S32
Graphene nanoplatelets	PVDF	12.4	24.11	S33
Ultrathin graphite foams	Epoxy	2.8	1.2	S34
Aligned multilayer graphene	Paraffin	16.75	7.04	S35
Graphene−multilayer graphene	Epoxy	5.1	10	S36
Graphite Nanoplatelet – CNT	Epoxy	4.6	27.4	S37
Exfoliated graphite	Epoxy	5.8	12.4	S38
Vertically aligned graphite network	TME	16.4	9.09	S39

Reticulated graphite nanoplatelets	PE	33.5	9.84	S40
Air-dried graphene skeleton	n-Docosane	9.87	10.52	S41
Melamine foam /GNP/Carbon Nanotubes	Octadecane	0.65	6.99	S42
CNTs sponge	Sebacic acid	7.27	4.85	S43
Chitosan/graphene aerogels	PEG	2.9	1.33	S44
Graphene skeleton	Paraffin wax	2.58	2.25	S45
Vertically aligned carbon fibers	Paraffin wax	0.77	1.81	S46
Expanded graphite	OP44/Natural rubber latex	3.4	6.52	S47
Carbon nanotube sponge	PEG	2.4	3.97	S48
3D network carbon	PEG	0.91	7.03	S49
High-quality conical graphene aerogels	Tetradecanol	4.54	2.89	S50
Graphene paper/graphene-foam composite	Stearic acid	1.72	0.21	S51
Expanded graphite	OBC/PW	17	9.68	S52
Assisted by ability of aramid nanofibers	PEG	4.26	4.85	S53
Van der Waals-bonded graphene clusters (VBGC)	Phase-change microcapsules	103	≈ 29	This work

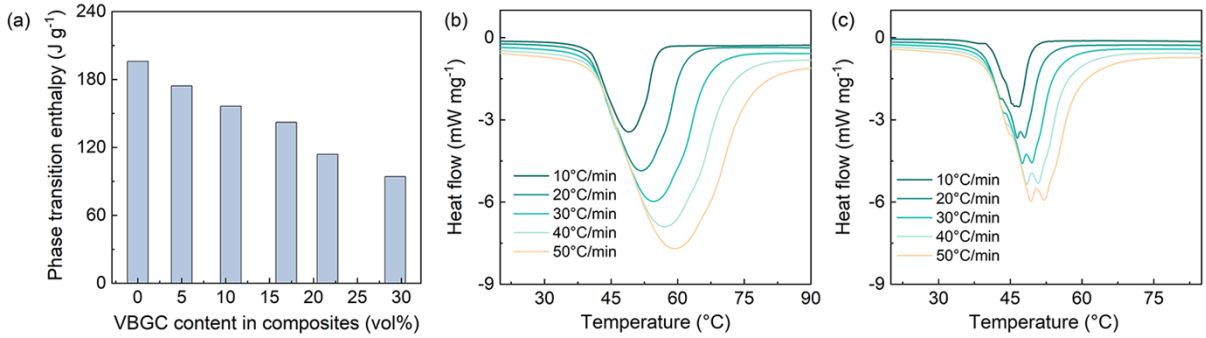

Fig. S6 (a) The calculated phase transition enthalpy of VBGC/PCMCs as a function of filler content. Differential scanning calorimetry (DSC) heating scan curves for (b) pure PCMC and (c) VBGC/PCMCs, with the heating rate varying from 10 to 50 °C min^{-1}.

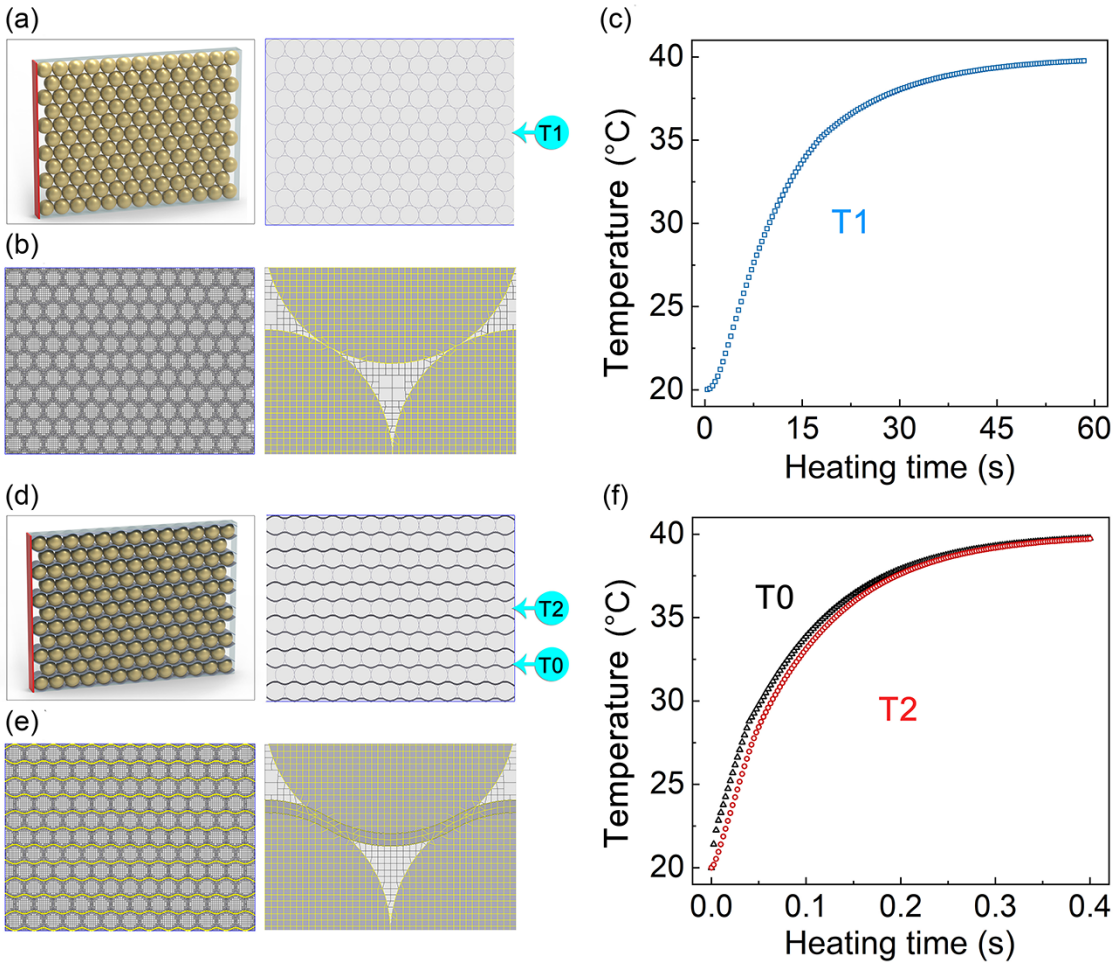

Fig. S7 (a) Schematic of the Icepak simulation models and (b) the corresponding cut-plane mesh for pure PCMC modules. (c) The temperature valuss of the T_1 as a function of the calculated time. (d) Schematic of the ANSYS simulation models and (e) the corresponding mesh generation for

VBGC/PCMC modules. (f) The temperature values of the T_0 and T_1 as a function of the calculated time.

To investigate the transient thermal response behavior of the pure PCMC and PCMC/VBGC, we conducted thermal simulation analyses using commercial computational fluid dynamics software (Icepak). Based on the structural features of pure PCMC and VBGC/PCMC, we established a simplified model, as shown in Fig. S7. Taking the pure PCMC model as an example (Fig. S7a–b), the dimensions of the simulation region were set to 2 mm × 2.2 mm × 0.24 mm, where the spherical PCMC was arranged in a hexagonal stacking pattern with a thermal conductivity of 0.5 W m^{-1} K^{-1}. In the VBGC/PCMC model (Fig. S7d–e), in addition to the spherical PCMC, we also introduced a heat transfer path composed of VBGC that traverses the entire model. Based on the predictions from the metal foam model, the equivalent thermal conductivity of the VBGC/PCMC heat pathway was set to 10^3 W m^{-1} K^{-1}.

The computational domain starts with an initial temperature of 20 °C, and adiabatic boundary conditions are stipulated. At the initiation of the transient analysis, a heat source with a constant temperature of 40 °C (depicted schematically as the red line in Fig. S7a and d) was introduced at the left sides of the two modules, resulting in the establishment of one-dimensional heat conduction through the PCMC and VBGC/PCMC. Consequently, as depicted in Fig. S7c and f, the VBGC/PCMC module achieves a steady state ($T_0 \approx T_2 \approx 39.8$ °C) in just 0.40 s, while the pure PCMC case requires a significantly longer time of 60 s. The temperature trend in Fig. S7f indicates that the VBGC component (T_0) experiences a faster and consistently higher increase compared to the matrix (T_2) until reaching the steady state, further affirming the pivotal role of VBGC as the heat pathway for enhancing the transient thermal response performance.

Table S4 A comparison of the thermal conductivity and the thermal effusivity of our VBGC/PCMC (29 vol%) with the latest reported carbon-based phase-change composites. Since some references omitted the density of the phase-change composites, we calculated the maximum probable thermal effusivity for the composites using the maximum density. This calculation assumes that the carbon-based fillers and the matrix are perfectly mixed without internal pores within the composite blocks.

Phase-change composites	**Thermal conductivity ($W\ m^{-1}\ K^{-1}$)**	**Thermal effusivity ($Jcm^{-3/2}(msK)^{-1/2}$)**	**Ref.**
Graphene framework/paraffin	1.46	14.4	S54
Hybridizing graphene aerogel/paraffin	1.82	15.5	S55
3D network carbon/PEG	0.69	9.34	S56
Boron nitride nanotube-rGO/PEG	0.43	9.73	S56
Cellulose-graphene aerogel/PEG	1.35	15.4	S57
Carbon aerogels/paraffin	0.427	6.56	S58
High-quality conical graphene aerogels/tetradecanol	4.54	28.6	S50
Carbon nanotube sponge/PEG	2.4	17.3	S48
Ultrathin-graphite foams-CNT//erythritol	4.1	44.4	S30
Ultrathin-graphite foams/erythritol	2.13	32.4	S34
Air-dried graphene skeleton/n-Docosane	9.87	39.8	S59
Anisotropic graphene aerogels/paraffin	8.87	38.3	S16
Melamine foam /GNP/carbon nanotubes/octadecane	0.65	11.5	S42
Expanded graphite/OBC/PW	17	55.8	S52
Melamine foam-rGO/paraffin	0.096	3.45	S60
Ultrathin-graphite foams/paraffin	3.54	24.7	S34
Graphene aerogels/octadecanol	4.28	28	S13
Reticulated graphite nanoplatelets/PE	33.5	87.8	S40
Vertically aligned carbon fibers/PW	0.77	12	S46
Graphene hybrid aerogels/octadecanol	5.92	35.6	S20
Oriented graphite sheets/stearic acid (SA)	35	69.7	S61
Carbon fibers / palmitic acid (PA)/ Olefin block copolymer (OBC)	5.84	29.5	S62

Graphene paper/graphene-foam composite/stearic acid	1.72	6	S51
Multi-layer graphene-Cu/octadecane	10.35	42	S63
Expanded graphite/OP44/Natural rubber latex	3.4	22.8	S47
CNTs sponge/Sebacic acid	7.27	27.8	S43
Chitosan/graphene aerogels/PEG	2.9	24.3	S44
Vertically aligned graphite network/TME	16.4	44.6	S39
Graphene skeleton/ paraffin	2.58	20.5	S45
Graphene oxide/paraffin	0.698	9.8	S64
Hybrid graphene aerogels/PEG	1.43	17.1	S17
VBGC/PCMC (29 vol%)	103	134	This work

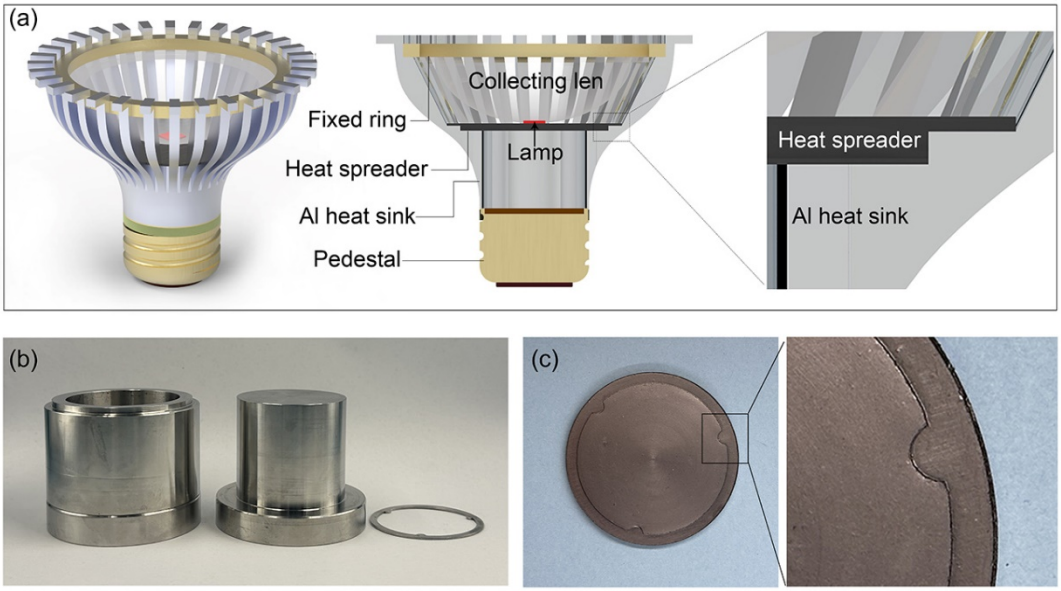

Fig. S8 (a) Schematic illustrating the test platform for cooling LED using a heat spreader. (b) The specialized molds are used to fabricate VBGC/PCMC, achieving custom-shaped interfaces compatible with Al heat sinks (c).

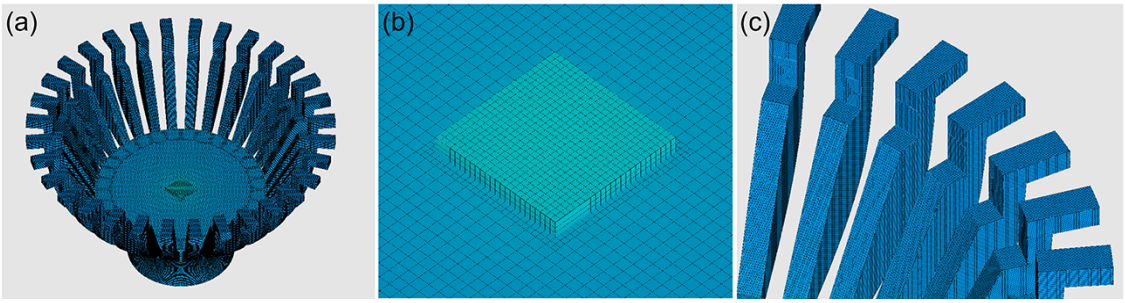

Fig. S9 (a) Thermal simulation model and (b and c) the corresponding mesh generation.

To gain a deeper insight into the thermal management properties of the heat spreaders, the commercial computational fluid dynamics software (Icepak) was employed to simulate the heat transfer process of the LED cooling system. The model setup is illustrated in Fig. S9, with the power density of the heater (LED chip) set at 32 W cm^{-2}. The overall system operated at a background temperature of 20 °C under standard atmospheric conditions (1 atm). The intricate parameters of the heater, heat sink, and the four heat spreaders are outlined in Table S5. In Fig. S10, the simulated overall

temperature cloud map and cross-sectional temperature distribution of the cooling system highlight the enhanced heat dissipation capability of our VBGC/PCMC as heat spreaders.

Table S5 The detailed parameters of the components in the simulated system.

	Size (cm^3)	Materials	κ ($W\ m^{-1}\ K^{-1}$)	C_p ($J\ g^{-1}\ K^{-1}$)
Heater	1 × 1 × 0.1	Al_2O_3	27	0.91
Heat sink	Sunflower	Aluminum	237	0.88
Heat spreader #1	Φ 4.0 × 0.2	Al_2O_3	28	0.91
Heat spreader #2	Φ 4.0 × 0.2	Si_3N_4	65	0.75
Heat spreader #3	Φ 4.0 × 0.2	AlN	181	0.85
Heat spreader #4	Φ 4.0 × 0.2	/	353	1.10

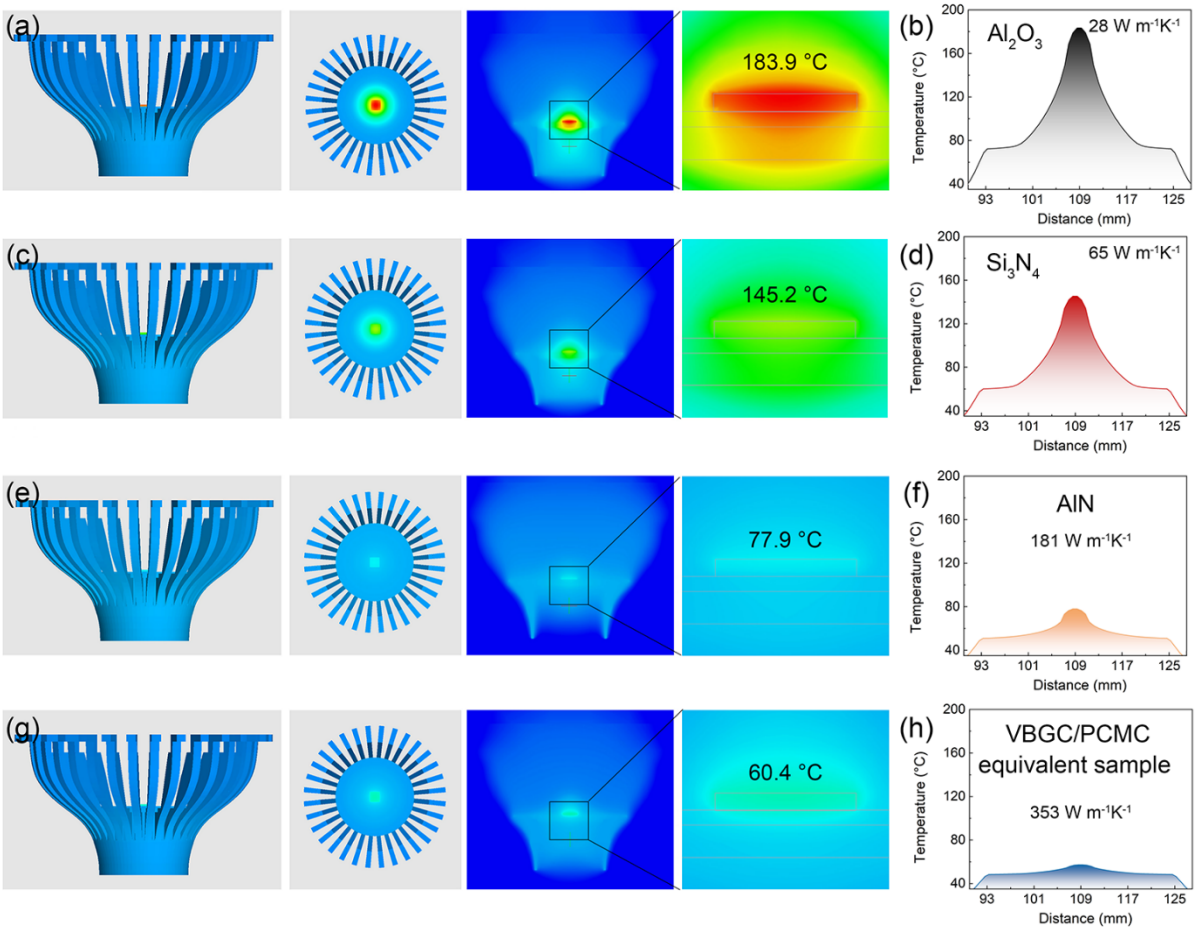

Fig. S10 (a) Simulated overall temperature cloud map and (b) cross-sectional temperature distribution of the cooling system using Al_2O_3 as the heat spreader. (c – h) The same results for cases of Si_3N_4, AlN and the VBGC/PCMC equivalent sample, respectively.

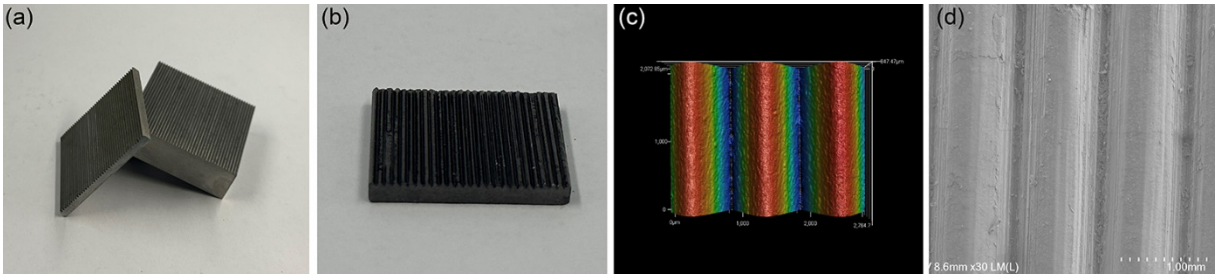

Fig. S11 (a) The specialized molds are used to fabricate P-VBGC/PCMC. The photograph and the microstructural images of as-prepared P-VBGC/PCMC.

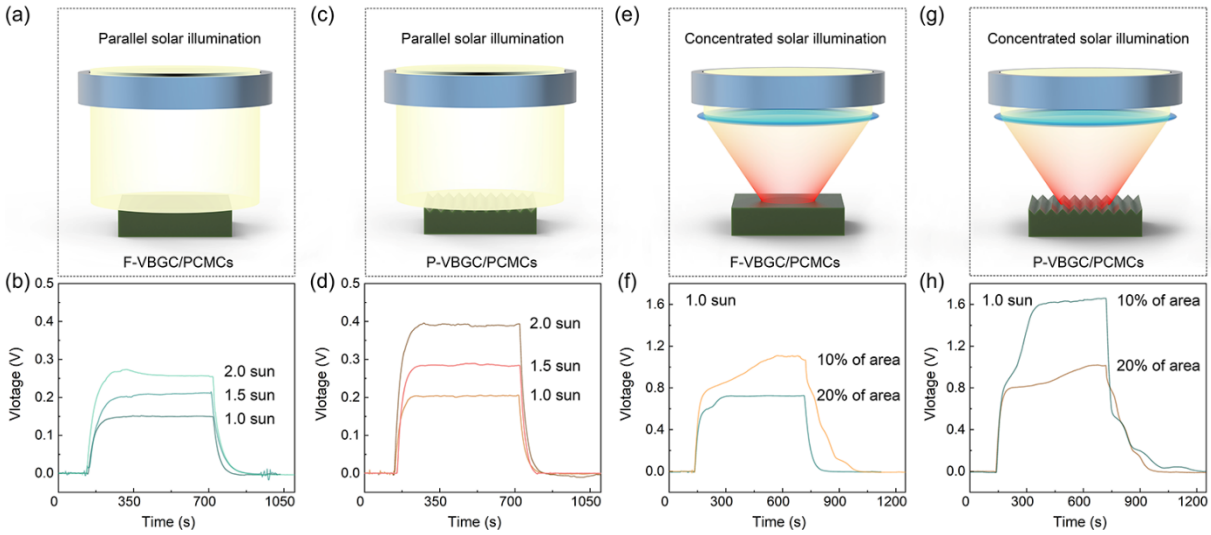

Fig. S12 Solar-thermal-electric conversion test involves the illumination method, the measured samples, and the collected open-circuit voltage: (a) Parallel solar illumination on F-VBGC/PCMC, (b) Parallel solar illumination on P-VBGC/PCMC, (c) Concentrated solar illumination on F-VBGC/PCMC, and (d) Concentrated solar illumination on P-VBGC/PCMC.

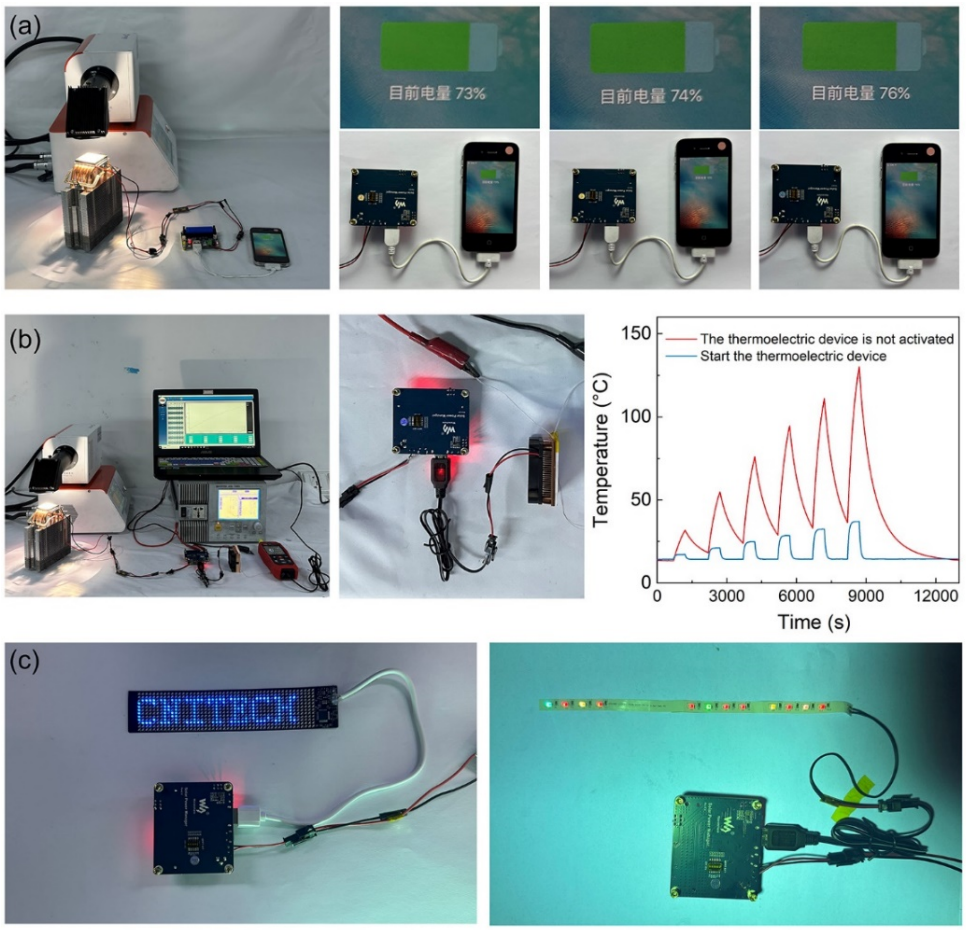

Fig. S13 (a) A thermoelectric device is used to provide power for charging a mobile phone. (b) The thermoelectric device drives the fan to cool the heating element. (c) The thermoelectric device generates power to illuminate the LED indicator light.

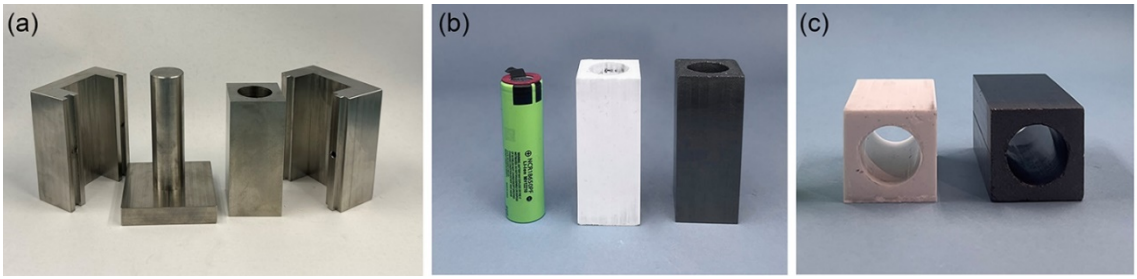

Fig. S14 (a) The specialized molds for preparing battery wrap using PCMC and VBGC/PCMC. (b–c) Photograph of the as-prepared PCMC and VBGC/PCMC wrap.

Reference:

1 L. Peng, Z. Xu, Z. Liu, Y. Guo, P. Li, C. Gao, *Adv. Mater.* 2017, **29**, 1700589.

2 L. G. Cançado, K. Takai, T. Enoki, M. Endo, Y. A. Kim, H. Mizusaki, A. Jorio, L. N. Coelho, R. Magalhães-Paniago, M. A. Pimenta, *Appl. Phys. Lett.* 2006, **88**, 163106.

3 G. Xin, H. Sun, T. Hu, H. R. Fard, X. Sun, N. Koratkar, T. Borca-Tasciuc, J. Lian, *Adv. Mater.* 2014, **26**, 4521-4526.

4 C. Teng, D. Xie, J. Wang, Z. Yang, G. Ren, Y. Zhu, *Adv. Funct. Mater.* 2017, **27**, 1700240.

5 Y. Agari, T. Uno, *J. Appl. Polym. Sci.* 1986, **32**, 5705-5712.

6 L. Lindsay, D. Broido, *Phys. Rev. B* 2010, **81**, 205441.

7 L. Girifalco, M. Hodak, R. S. Lee, *Phys. Rev. B* 2000, **62**, 13104.

8 L. Lindsay, D. A. Broido, N. Mingo, *Phys. Rev. B* 2011, **83**, 235428.

9 A. Rajabpour, S. M. Vaez Allaei, *Appl. Phys. Lett.* 2012, **101**, 053115.

10 X. Zeng, Y. Yao, Z. Gong, F. Wang, R. Sun, J. Xu, C.-P. Wong, *Small* 2015, **11**, 6205-6213.

11 J. Hu, Y. Huang, Y. Yao, G. Pan, J. Sun, X. Zeng, R. Sun, J.-B. Xu, B. Song, C.-P. Wong, *ACS Appl. Mater. Interfaces* 2017, **9**, 13544-13553.

12 P. Liu, X. Li, P. Min, X. Chang, C. Shu, Y. Ding, Z.-Z. Yu, *Nano-Micro Lett.* 2020, **13**, 22.

13 J. Yang, X. Li, S. Han, R. Yang, P. Min, Z.-Z. Yu, *J. Mater. Chem. A* 2018, **6**, 5880-5886.

14 X.-H. Li, P. Liu, X. Li, F. An, P. Min, K.-N. Liao, Z.-Z. Yu, *Carbon* 2018, **140**, 624-633.

15 M. Qin, Y. Xu, R. Cao, W. Feng, L. Chen, *Adv. Funct. Mater.* 2018, **28**, 1805053.

16 P. Min, J. Liu, X. Li, F. An, P. Liu, Y. Shen, N. Koratkar, Z.-Z. Yu, *Adv. Funct. Mater.* 2018, **28**, 1805365.

17 J. Yang, G.-Q. Qi, Y. Liu, R.-Y. Bao, Z.-Y. Liu, W. Yang, B.-H. Xie, M.-B. Yang, *Carbon* 2016, **100**, 693-702.

18 G. Lian, C.-C. Tuan, L. Li, S. Jiao, Q. Wang, K.-S. Moon, D. Cui, C.-P. Wong, *Chem. Mater.* 2016, **28**, 6096-6104.

19 J. Gong, Z. Liu, J. Yu, D. Dai, W. Dai, S. Du, C. Li, N. Jiang, Z. Zhan, C.-T. Lin, *Compos. Part A Appl. Sci. Manuf.* 2016, **87**, 290-296.

20 J. Yang, X. Li, S. Han, Y. Zhang, P. Min, N. Koratkar, Z.-Z. Yu, *J. Mater. Chem. A* 2016, **4**, 18067-18074.

21 H. S. Kim, H. S. Bae, J. Yu, S. Y. Kim, *Sci. Rep.* 2016, **6**, 26825.

22 A. M. Marconnet, N. Yamamoto, M. A. Panzer, B. L. Wardle, K. E. Goodson, *ACS Nano* 2011, **5**, 4818-4825.

23 Z. Barani, A. Mohammadzadeh, A. Geremew, C.-Y. Huang, D. Coleman, L. Mangolini, F. Kargar, A. A. Balandin, *Adv. Funct. Mater.* 2020, **30**, 1904008.

24 Z. Wu, C. Xu, C. Ma, Z. Liu, H.-M. Cheng, W. Ren, *Adv. Mater.* 2019, **31**, 1900199.

25 X. Shen, Z. Wang, Y. Wu, X. Liu, Y.-B. He, Q. Zheng, Q.-H. Yang, F. Kang, J.-K. Kim, *Mater. Horizons* 2018, **5**, 275-284.

26 F. An, X. Li, P. Min, H. Li, Z. Dai, Z.-Z. Yu, *Carbon* 2018, **126**, 119-127.

27 H. Hou, W. Dai, Q. Yan, L. Lv, F. E. Alam, M. Yang, Y. Yao, X. Zeng, J.-B. Xu, J. Yu, N. Jiang, C.-T. Lin, *J. Mater. Chem. A* 2018, **6**, 12091-12097.

28 F. An, X. Li, P. Min, P. Liu, Z.-G. Jiang, Z.-Z. Yu, *ACS Appl. Mater. Interfaces* 2018, **10**, 17383-17392.

29 X. Shen, Z. Wang, Y. Wu, X. Liu, Y.-B. He, J.-K. Kim, *Nano letters* 2016, **16**, 3585-3593.

30 I. Kholmanov, J. Kim, E. Ou, R. S. Ruoff, L. Shi, *ACS Nano* 2015, **9**, 11699-11707.

31 W. Dai, J. Yu, Y. Wang, Y. Song, F. E. Alam, K. Nishimura, C.-T. Lin, N. Jiang, *J. Mater. Chem. A* 2015, **3**, 4884-4891.

32 H. Jung, S. Yu, N.-S. Bae, S. M. Cho, R. H. Kim, S. H. Cho, I. Hwang, B. Jeong, J. S. Ryu, J. Hwang, S. M. Hong, C. M. Koo, C. Park, *ACS Appl. Mater. Interfaces* 2015, **7**, 15256-15262.

33 M. Shtein, R. Nadiv, M. Buzaglo, K. Kahil, O. Regev, *Chem. Mater.* 2015, **27**, 2100-2106.

34 H. Ji, D. P. Sellan, M. T. Pettes, X. Kong, J. Ji, L. Shi, R. S. Ruoff, *Energy Environ. Sci.* 2014, **7**, 1185-1192.

35 Q. Li, Y. Guo, W. Li, S. Qiu, C. Zhu, X. Wei, M. Chen, C. Liu, S. Liao, Y. Gong, A. K. Mishra, L. Liu, *Chem. Mater.* 2014, **26**, 4459-4465.

36 K. M. F. Shahil, A. A. Balandin, *Nano Lett.* 2012, **12**, 861-867.

37 A. Yu, P. Ramesh, X. Sun, E. Bekyarova, M. E. Itkis, R. C. Haddon, *Adv. Mater.* 2008, **20**, 4740-4744.

38 S. Ganguli, A. K. Roy, D. P. Anderson, *Carbon* 2008, **46**, 806-817.

39 S. Wu, T. Li, M. Wu, J. Xu, J. Chao, Y. Hu, T. Yan, Q.-Y. Li, R. Wang, *ACS Appl. Mater. Interfaces* 2021, **13**, 19200-19210.

40 T. Li, M. Wu, S. Wu, S. Xiang, J. Xu, J. Chao, T. Yan, T. Deng, R. Wang, *Nano Energy* 2021, **89**, 106338.

41 J. Huang, J. Su, M. Weng, L. Xiong, P. Wang, Y. Liu, X. Lin, Y. Min, *Sol. Energy Mater Sol. Cells* 2022, **245**, 111872.

42 J. Deng, Y. Kou, H. Liu, M. Yang, K. Sun, R. Joshi, Q. Shi, *ACS Appl. Energy Mater.* 2023, **6**, 7457-7567.

43 Q. Zhang, J. Liu, *Sol. Energy Mater Sol. Cells* 2018, **179**, 217-222.

44 H.-Y. Zhao, C. Shu, X. Wang, P. Min, C. Li, F.-L. Gao, X. Li, Z.-Z. Yu, *Adv. Funct. Mater.* 2023, **33**, 2302527.

45 Y. Lin, Q. Kang, H. Wei, H. Bao, P. Jiang, Y.-W. Mai, X. Huang, *Nano-Micro Lett.* 2021, **13**, 180.

46 N. Sheng, R. Zhu, K. Dong, T. Nomura, C. Zhu, Y. Aoki, H. Habazaki, T. Akiyama, *J. Mater. Chem. A* 2019, **7**, 4934-4940.

47 K. Yang, Z. Ling, X. Fang, Z. Zhang, *J. Energy Chem.* 2023, **66**, 107486.

48 W. Aftab, A. Mahmood, W. Guo, M. Yousaf, H. Tabassum, X. Huang, Z. Liang, A. Cao, R. Zou, *Energy Stor. Mater.* 2019, **20**, 401-409.

49 X. Chen, H. Gao, M. Yang, W. Dong, X. Huang, A. Li, C. Dong, G. Wang, *Nano Energy* 2018, **49**, 86-94.

50 H.-Y. Zhao, C. Shu, P. Min, C. Li, W. Deng, J. Yang, X. Li, Z.-Z. Yu, *J. Mater. Chem. A* 2022, **10**, 22488-22499.

51 G. Liang, J. Zhang, S. An, J. Tang, S. Ju, S. Bai, D. Jiang, *Carbon* 2021, **176**, 11-20.

52 S. Wu, T. Li, M. Wu, J. Xu, Y. Hu, J. Chao, T. Yan, R. Wang, *J. Mater. Chem. A* 2020, **8**, 20011-20020.

53 J. Gao, B. Zhou, C. Liu, C. He, Y. Feng, C. Liu, *Chem. Eng. J.* 2023, **475**, 146087.

54 F. Xue, Y. Lu, X.-d. Qi, J.-h. Yang, Y. Wang, *Chem. Eng. J.* 2019, **365**, 20-29.

55 J. Yang, G.-Q. Qi, R.-Y. Bao, K. Yi, M. Li, L. Peng, Z. Cai, M.-B. Yang, D. Wei, W. Yang, *Energy Stor. Mater.* 2018, **13**, 88-95.

56 M. Wang, T. Zhang, D. Mao, Y. Yao, X. Zeng, L. Ren, Q. Cai, S. Mateti, L. H. Li, X. Zeng, G. Du, R. Sun, Y. Chen, J.-B. Xu, C.-P. Wong, *ACS Nano* 2019, **13**, 7402-7409.

57 J. Yang, E. Zhang, X. Li, Y. Zhang, J. Qu, Z.-Z. Yu, *Carbon* 2016, **98**, 50-57.

58 Y. Wei, J. Li, F. Sun, J. Wu, L. Zhao, *Green Chem.* 2018, **20**, 1858-1865.

59 J. Wang, W. Li, X. Zhang, *J. Mater. Sci. Technol.* 2023, **178**, 179.

60 J.-h. Jing, H.-y. Wu, Y.-w. Shao, X.-d. Qi, J.-h. Yang, Y. Wang, *ACS Appl. Mater. Interfaces* 2019, **11**, 19252-19259.

61 S. Wu, T. Li, Z. Tong, J. Chao, T. Zhai, J. Xu, T. Yan, M. Wu, Z. Xu, H. Bao, *Adv. Mater.* 2019, **31**, 1905099.

62 P. Zhang, Y. Wang, Y. Qiu, H. Yan, Z. Wang, Q. Li, *Appl. Energy* 2024, **358**, 122546.

63 A. L. Cottrill, A. T. Liu, Y. Kunai, V. B. Koman, A. Kaplan, S. G. Mahajan, P. Liu, A. R. Toland, M. S. Strano, *Nat. Commun.* 2018, **9**, 664.

64 K. Yuan, J. Liu, X. Fang, Z. Zhang, *J. Mater. Chem. A* 2018, **6**, 4535-4543.